Petroleum Science 23 (2026) 1804–1816

Contents lists available at ScienceDirect

Petroleum Science

journal homepage: www.keaipublishing.com/en/journals/petroleum-science

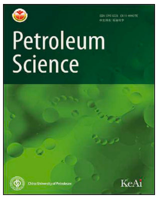

Original Paper

Boosted organic carbon accumulation in the Late Cretaceous Songliao Basin during marine incursion events

Ke-Rui Wu [a,b], Yu Sun [a,b,*], Da-Ming Yang [a,b,**], Fu-Li Fang [b], Bai-Quan Yan [c], Jie Zhou [b], Tao Yu [c]

[a] *State Key Laboratory of Continental Shale Oil, Northeast Petroleum University, Daqing, 163318, Heilongjiang, China*
[b] *School of Earth Sciences, Northeast Petroleum University, Daqing, 163318, Heilongjiang, China*
[c] *Sanya Offshore Oil & Gas Research Institute, Northeast Petroleum University, Sanya, 572025, Hainan, China*

ARTICLE INFO

Article history:
Received 27 August 2025
Received in revised form
22 November 2025
Accepted 15 March 2026
Available online 18 March 2026

Edited by Xiu-Fang Hu

Keywords:
Organic carbon accumulation
Marine incursion events
Qingshankou Formation
Songliao Basin
Lacustrine shale oil and gas
Paleolake

ABSTRACT

Although the Late Cretaceous marine incursion events (MI) significantly boosted organic carbon (OC) accumulation in the Songliao Basin, their net effects and accumulation mechanisms have long been debated. By integrating high-resolution geological data, multi-proxy paleoenvironmental analysis, and a machine learning-based approach for TOC prediction in Member 1 of the Qingshankou Formation, we reveal that total OC sediment accumulation rates (OCSAR) during high-intensity MI (HMI) increased by 28.8% compared to low-intensity MI (LMI) intervals, with the areal OCSAR of the study area rising from 0.43×10^{-2} to 0.55×10^{-2} GtC/(Myr·km^2). The OC accumulation models during HMI and LMI are established: driven by the interplay of seawater influxes, basin morphology, and terrigenous inputs, which collectively modulated the bacterial sulfate reduction, redox conditions, and nutrient availability in the water column, the growth rate of areal OCSAR exhibited pronounced spatial heterogeneity, defining four distinct zones (I–IV). The validation case from the Nenjiang Formation demonstrates the robustness of the models. These findings establish MI as a global amplifier of OC burial in mega-paleolake systems and redefine resource development frameworks for lacustrine shales within MI sequences.

1. Introduction

The relentless global pursuit of energy security continues to drive the development of unconventional shale resources (Allen et al., 2013; Hackley and Cardott, 2016). While extensive knowledge of marine shale systems has underpinned the North American shale revolution, unlocking the vast potential of lacustrine shale oil, which is characterized by significant geological heterogeneity and complex lithofacies, is emerging as a critical frontier for securing autonomous energy supplies. This is particularly vital for nations reliant on lacustrine basins, such as China (Zou et al., 2013, 2022). Within these systems, the distribution and accumulation of organic carbon (OC)—the precursor to hydrocarbon generation and retention—exhibits significant spatial heterogeneity (Hu et al., 2021). A mechanistic understanding of OC accumulation efficiency and its spatial variability in rapidly deposited lake environments is therefore essential, both for academic advancement and as a foundation for precise resource assessment, sweet-spot identification, and optimized development strategies (Li et al., 2024).

Marine incursion events (MI)—a widespread geological phenomenon across various spatiotemporal scales—exhibit mechanistically debated net effects on lacustrine OC accumulation (Jones et al., 2018; Xiao et al., 2025). While seawater influxes profoundly reshape lacustrine biogeochemical cycles, they trigger contradictory effects on OC accumulation. These influxes deliver key nutrients (e.g., phosphorus (P) and copper (Cu)), stimulating primary productivity and enhancing OC accumulation efficiency through water column stabilization (Zhu et al., 2023; Chen et al., 2024). Conversely, MI promote bacterial sulfate reduction and thus

---

[*] Corresponding author.
[**] Corresponding author.
E-mail addresses: sunyunepu@nepu.edu.cn (Y. Sun), yangdm@nepu.edu.cn (D.-M. Yang).

Peer review under the responsibility of China University of Petroleum (Beijing).

https://doi.org/10.1016/j.petsci.2026.03.033

enhance organic matter (OM) remineralization (Ding et al., 2024; Gao et al., 2025). Additionally, MI reduce the photic zone, limiting photosynthetic carbon fixation (Liu et al., 2013), and can induce water column acidification that suppresses carbon uptake. This complexity implies spatially heterogeneous OC accumulation efficiency during MI, necessitating integrated, multi-proxy investigations.

The Songliao Basin, one of Earth's largest lake systems during the Late Cretaceous, preserves continuous, high-resolution sedimentary records (Scott et al., 2012). Critically, recurrent MI occurred at the base of Member 1 of the Qingshankou Formation (K_2qn^1) (Jones et al., 2018). Its high sensitivity to global paleoclimate change renders it an ideal natural laboratory for studying MI–OC cycle coupling processes (Wang et al., 2013). By synthesizing multidisciplinary datasets, we quantify total OC accumulation and OC sediment accumulation rates (OCSAR), and characterize paleoenvironmental change in the K_2qn^1 during high-intensity MI (HMI) and low-intensity MI (LMI) intervals. Our objectives are threefold: (i) to reveal the mechanisms controlling OC accumulation in mega-paleolakes during MI; (ii) to establish generalized models for these processes; and (iii) to evaluate the implications for global carbon sink dynamics and lacustrine shale hydrocarbon exploration.

2. Geological background

The Songliao Basin, the largest continental petroliferous basin in Northeast China (Fig. 1(a)(b); Li et al., 2021), extends approximately 260,000 km^2 in a NE–SW orientation. The basin tectonic evolution comprises four distinct stages: Late Jurassic thermal rifting, Early Cretaceous extensional faulting, middle Early Cretaceous thermal subsidence, and Late Cretaceous structural inversion (Feng et al., 2010). Based on basement morphology and fault distribution, the basin is subdivided into six tectonic units, comprising the Central Depression (Fig. 1(c); Feng et al., 2010). The Upper Cretaceous Qingshankou Formation (K_2qn), stratigraphically between the Quantou and Yaojia formations, is divided into the Member 1 (K_2qn^1) and the Members 2 and 3 (collectively referred to as K_2qn^{2+3}) in ascending order. Deposition of K_2qn^1 initiated at ~91.82 Ma (Wu et al., 2022), coinciding with an abrupt lake-level rise and a sedimentary facies shift from fluvial to deltaic–lacustrine sediments. Lacustrine sediments are predominantly distributed within the Central Depression, the northern Southeastern Uplift, and the southern Northeastern Uplift (Fig. 1(c); Liu et al., 2023a).

The debate surrounding the MI during the K_2qn^1 remains unresolved, with key controversies focusing on: (i) whether the MI actually occurred, and (ii) the extent of its incursion. However, multi-disciplinary evidence demonstrates that although intermittent MI did not fundamentally alter the freshwater nature of the paleolake, these events played a critical role in regulating biogeochemical cycles. The evidence includes: paleoenvironmental proxies indicative of salinity or redox conditions (e.g., elevated Gammacerane index (GI) and pristane/phytane (Pr/Ph) ratios; Xu et al., 2019), the presence of marine-derived microfossils such as foraminifers (Xi et al., 2016) and dinoflagellates (Lv et al., 2023), distinctive biomarker concentrations (e.g., dinosteranes and 24-*n*-propylcholestanes; Hou et al., 2000; Hu et al., 2015), and isotopic signatures ($\delta^{34}S$ values approaching Cretaceous seawater; $^{87}Sr/^{86}Sr$ ratios as low as 0.7076 to 0.7080; Huang et al., 2013; Liu et al., 2023b; Chen et al., 2024). Multi-proxy evidence identifies the Yitong Graben as a possible pathway for seawater influxes, with seawater advancing from the southeast to the northwest (Fig. 1(d); Lv et al., 2023). Current research indicates that MI signals are widely distributed in deep lakes, as evidenced by multiple wells: NGN2 in the Southeastern Uplift shows higher GI and lower Pr/Ph ratios (Xu et al., 2019); ZY1S in the Sanzhao Sag exhibits low $^{87}Sr/^{86}Sr$ ratios (Chen et al., 2024); SK-1s in the Gulong Sag contains higher 24-*n*-propylcholestane values (Hu et al., 2015); and GY8HC is rich in dinoflagellate fossils (Lv et al., 2023).

Integrated geochemical data—including TOC, stable isotopes, and biomarkers (Han et al., 2011; Huang et al., 2013; Hu et al., 2015; Jones et al., 2018)—coupled with sedimentological evidence (Wu et al., 2022), reveal a HMI between 91.43 Ma and 91.71 Ma. The HMI interval is characterized by more frequent and pronounced signals of MI influences, contrasting sharply with the preceding LMI (90.91–91.43 Ma), which was dominated by terrigenous and lake sediments (Fig. 1(e)).

3. Materials and methods

3.1. Data and sources

A comprehensive dataset was established to quantify total OC accumulation and develop predictive models. For the K_2qn^1, the database integrates the following data types: high-resolution measured TOC values from 39 wells; maximum pyrolysis temperature ($T_{\max}$) data from 18 wells; vitrinite reflectance (R_o) data from 8 wells; total sulfur (TS) data from 6 wells; trace elements from 7 wells; and organic geochemical proxies from 4 wells (Table S1–S3 in Supporting Information S1). To address spatial heterogeneity in well distribution, multiple logs from 9 additional wells were incorporated. Machine learning methods were subsequently employed to predict TOC variations across these wells (see Section 3.2), thereby enhancing the robustness of the OC accumulation mechanisms and model frameworks.

To evaluate the model's generalizability, we incorporated high-resolution measured TOC values and R_o data from four additional wells, which were obtained from Members 1 and 2 of the Upper Cretaceous Nenjiang Formation (K_2n).

3.2. TOC content prediction based on XGBoost algorithm

The XGBoost algorithm, an advanced gradient-boosting framework, was employed for TOC prediction. This method iteratively builds an ensemble of weak learners (decision trees). Each new tree is designed to correct the residuals (negative gradients) of the current ensemble, with the final prediction constituting a weighted summation of all trees. The algorithm enhanced predictive accuracy through two key mechanisms: (i) the integration of structural regularization terms into its objective function to control model complexity explicitly, and (ii) the utilization of second-order Taylor expansions of the loss function to precisely approximate gradient directions (Chen and Guestrin, 2016). We applied this framework to predict TOC content in 9 target wells (Table S2 in Supporting Information S1).

In TOC prediction, gamma ray (GR), acoustic (AC), compensated neutron log (CNL), density (DEN), and resistivity (RT) all provide valuable information (for detailed interpretation, see Section 2 in Supporting Information S1), but no single curve can reliably predict TOC alone. In practical applications, integrated methods such as machine learning algorithms (e.g., the XGBoost algorithm) are commonly employed to compensate for the limitations of individual curves, handle nonlinear relationships, and improve prediction accuracy (Lai et al., 2024). The training dataset comprised high-resolution measured TOC and corresponding multi-log curves—including GR, AC, CNL, DEN, and RT—from over 30 geographically diverse wells. This methodology mitigates spatial sampling bias and effectively captures the complex, non-linear mechanisms governing OC accumulation.

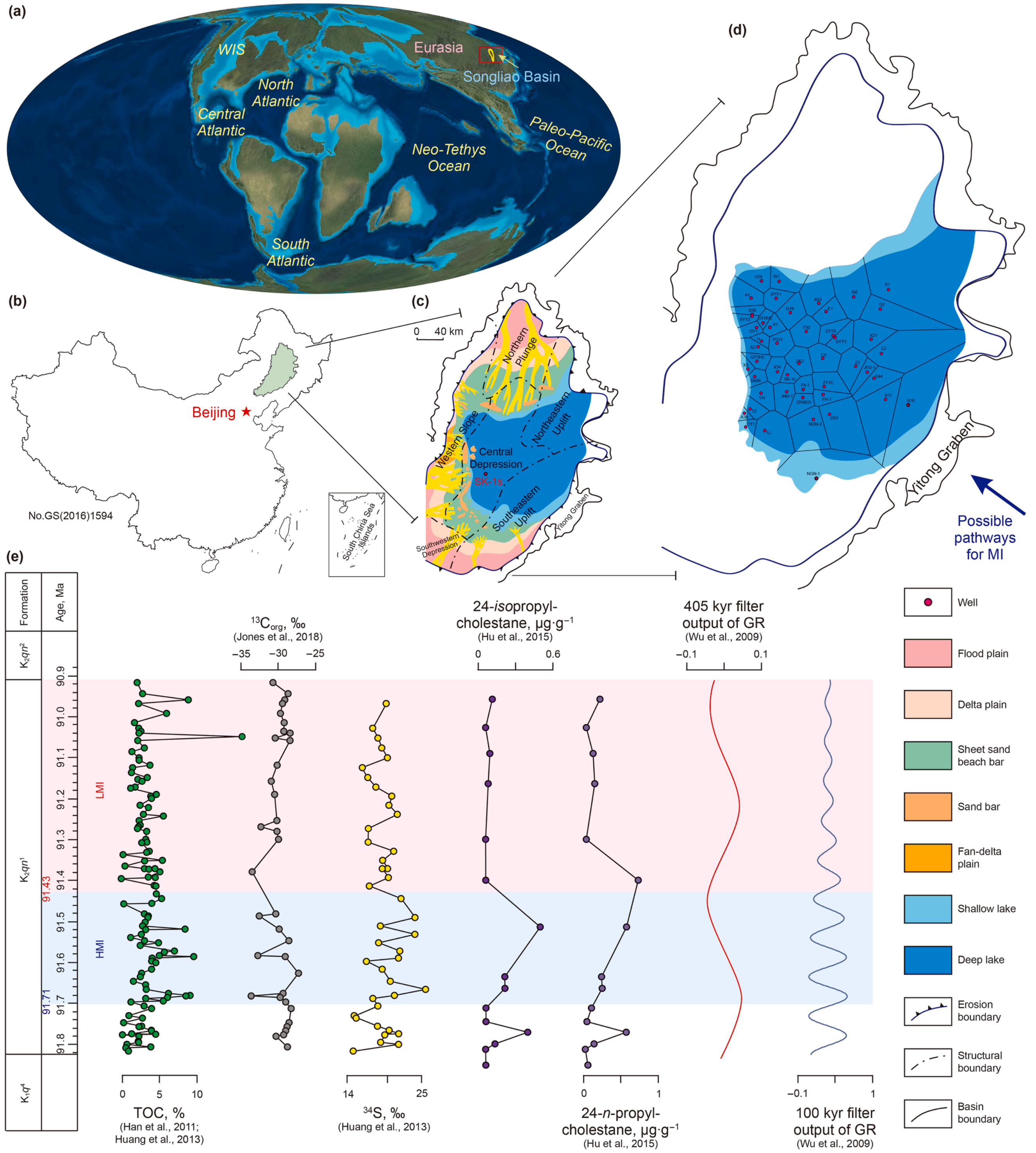

Fig. 1. **(a)** Paleogeographic reconstruction for Late Cretaceous ~90 Ma (Byrum and Lieberman, 2021), **(b)** location of the Songliao Basin in NE China, **(c)** depositional systems of the K_2qn^1 (Liu et al., 2023a), **(d)** study area and thiessen polygons distribution, **(e)** paleoenvironmental proxies of Well SK-1s during HMI and LMI, date from Wu et al. (2009), Han et al. (2011), Huang et al. (2013), Hu et al. (2015), and Jones et al. (2018). WIS: Western Interior Seaway.

3.3. Time series analysis methods

Cyclostratigraphy commonly utilizes paleoclimate proxies to identify Milankovitch cycles within stratigraphic records (Wu et al., 2009). Variations in the GR curve are highly sensitive to the concentration of radioactive elements within the strata (Santos et al., 2022). TOC values serve as an effective proxy for changes in the sedimentary environment (Huang et al., 2021). Consequently, both GR and TOC are exceptionally suitable as proxies for tracing paleoclimatic and paleoenvironmental cycles (for detailed interpretation, see Section 3 in Supporting Information S1). Utilizing paleoclimate proxies from multiple wells and the Acycle 2.7 software, we applied time series analysis to establish an astronomical time scale (ATS). The workflow consisted of three main stages: (i) Preprocessing: GR data were processed using the LOWESS method (Cleveland, 1979) to remove non-stationary noise; (ii) Spectral Analysis: The Multi-Taper Method (MTM) spectral estimator (Thomson, 1982) and robust first-order autoregressive AR(1) red noise models were applied to identify significant periodicities. Signals exceeding the 90% confidence level were selected and calibrated against the La2010d astronomical solution (Laskar et al., 2011) to detect Milankovitch signals (e.g., eccentricity, obliquity, precession); (iii) Cycle Extraction: Astronomical cycles were extracted using 2π tapers and the Fast Fourier Transform (FFT) (Li et al., 2019). All procedures followed the methodology detailed in Li et al. (2019).

Utilizing the GR and measured TOC curves, the resultant ATS was applied to delineate depth corresponding to HMI and LMI periods. Corresponding TOC values were subsequently aggregated for these chronostratigraphically defined intervals (for detailed interpretation, see Section 3 in Supporting Information S1).

3.4. Calculation of total OC accumulation and its SAR

Leveraging a preliminary dataset and DF-GVision 4.2 software, we determined the geographic coordinates of individual wells. These coordinates were imported into the ArcGIS platform, where Voronoi tessellation (Fig. 1(d)) was employed to delineate well-specific control areas (polygons) (Ma et al., 2022). The measured TOC values (TOCpre, present TOC) reflect point-specific measurements of OC content. These data served as the basis for reconstructing the total OC accumulation within the target stratigraphic unit. Given that the K_2qn^1 represents a highly mature source rock, a portion of its initial TOC (TOC_{ini}) has been converted to hydrocarbons and migrated to adjacent strata. To address the resulting underestimation of this transformation loss, we employed an empirical relationship between T_{max} and EASY%R_o (a method to calculate R_o) established by Zhang et al. (2024) for the K_2qn^1. This relationship enables the derivation of a restoration coefficient (K), which is subsequently applied to reconstruct the TOC_{ini}. By using the following formulas:

$$R_o = 0.0151 \times T_{max} - 5.9127 \tag{1}$$

$$K = R_o^2 - 0.76 \times R_o + 1.13 \tag{2}$$

$$TOC_{ini} = K \times TOC_{pre} \tag{3}$$

For wells lacking measured EASY%R_o or T_{max} values due to data limitations, we assigned the mean values from adjacent wells (Table S2 in Supporting Information S1). Subsequently, the following relationship was applied (Ma et al., 2022):

$$m_{OC} = \sum_{X=1}^{48} \left\{ \sum_{i=1}^{n} \left[\rho_{sh} \times P_{sh} \times (TOC_{ini})_i \times (1 - F_p) \times H_i / H_{Xd} \right] \times H_X \times S_X \right\} \tag{4}$$

Where m_{OC} is the total OC accumulation, ρ_{sh} denotes the bulk density of black shale (approximately 2600 kg/m^3), P_{sh} denotes the volumetric fraction of black shale within the formation (Ma et al., 2022; Lv et al., 2025a), F_p is the fraction of recycled petrogenic OM (~10%) (Sun et al., 2019), H_i denotes the controlled depth interval of $(TOC_{ini})_i$, H_{Xd} denotes the burial depth range of individual wells, S_X corresponds to the well-specific control area, and H_X denotes distinct average thicknesses of S_X. Following the calculation of total OC accumulation within the K_2qn^1 for both HMI and LMI intervals, we calculated OCSAR (in GtC/Myr), areal OCSAR (in 10^{-2} GtC/(Myr·km^2)), absolute change in OCSAR (ΔOCSAR, in 10^{-2} GtC/(Myr·km^2)) and growth rates of areal OCSAR (in %). By using the following formulas:

$$\text{OCSAR} = \text{total OC accumulation/Myr} \tag{5}$$

$$\text{areal OCSAR} = (\text{OC accumulation})_X / (S_X \cdot \text{Myr}) \tag{6}$$

$$\Delta\text{OCSAR} = (\text{OCSAR}_{\text{HMI}})_X - (\text{OCSAR}_{\text{LMI}})_X \tag{7}$$

$$\text{growth rates of areal OCSAR} = [(\text{areal OCSAR}_{\text{HMI}})_X - (\text{areal OCSAR}_{\text{LMI}})_X] / (\text{areal OCSAR}_{\text{LMI}})_X \tag{8}$$

4. Results

4.1. Results of TOC prediction based on the XGBoost

Using the XGBoost machine learning framework, we obtained high-resolution predictions of TOC content across 9 wells (D7, F50, G19, P331, R8, S1, S11, S16, S44; Table S2 in Supporting Information S1). The model demonstrated exceptional performance, as evidenced by a coefficient of determination (R^2) of 0.93 on the training dataset (Fig. 2(a)), which indicates its robust capacity to capture the fundamental patterns governing TOC distribution. Moreover, evaluation on an independent test set confirmed strong generalization capability, with an R^2 value of 0.86 (Fig. 2(b)). The close alignment between training and testing performance indicates that the model successfully captures the complex, nonlinear relationships controlling TOC values within these heterogeneous formations.

4.2. Establishment of interwell ATS

Take the Well GY8HC as an example, spectral analysis identified multiple high-confidence (>90%) periodic signals (0.025, 0.086, 0.12, 0.29, 0.42, 0.53, and 0.59 cycles/m). Given a cyclic thickness product of 1, the corresponding sedimentary thicknesses are 40 m, 11.62 m, 8.33 m, 3.44 m, 2.38 m, 1.88 m, and 1.69 m. The thickness ratios of 40:(11.62–8.33):(3.44–2.38):(1.88–1.69) approximate 20:5:2:1, which aligns with the theoretical ratios of Milankovitch cycles and indicates the preservation of long eccentricity (~405 kyr), short eccentricity (~100 kyr), obliquity (~40 kyr), and precession (~20 kyr) signals (Fig. 3(b)); While in Well C6, the high-confidence periodic signals are 0.03, 0.1, 0.13, 0.55, 0.59 cycles/m. The sedimentary thickness ratios of approximately 20:5:1 (corresponding to 33.33:(10–7.7):(1.82–1.68)) indicate the preservation of the long-eccentricity (~405 kyr), short-eccentricity (~100 kyr), and precession (~20 kyr) cycles (Fig. 3(c)). This methodology was systematically applied to other wells in the study area, establishing a robust interwell ATS correlation framework that enables high-resolution chronostratigraphic analysis for the basin (Fig. S1–S3 in Supporting Information S1).

4.3. Total OC accumulation and OCSAR for the LMI and HMI

The study area covered approximately 6.50×10^4 km^2, equivalent to one-fourth of the present-day Songliao Basin. Our calculations show that total OC accumulation during LMI intervals reached 143.2 GtC, compared to 99.9 GtC during HMI. The OCSAR increased significantly from 276.9 GtC/Myr during LMI to 356.8 GtC/Myr during HMI (Fig. 4(a)), demonstrating that MI boosted OC accumulation efficiency in this mega-paleolake system. Furthermore, the areal

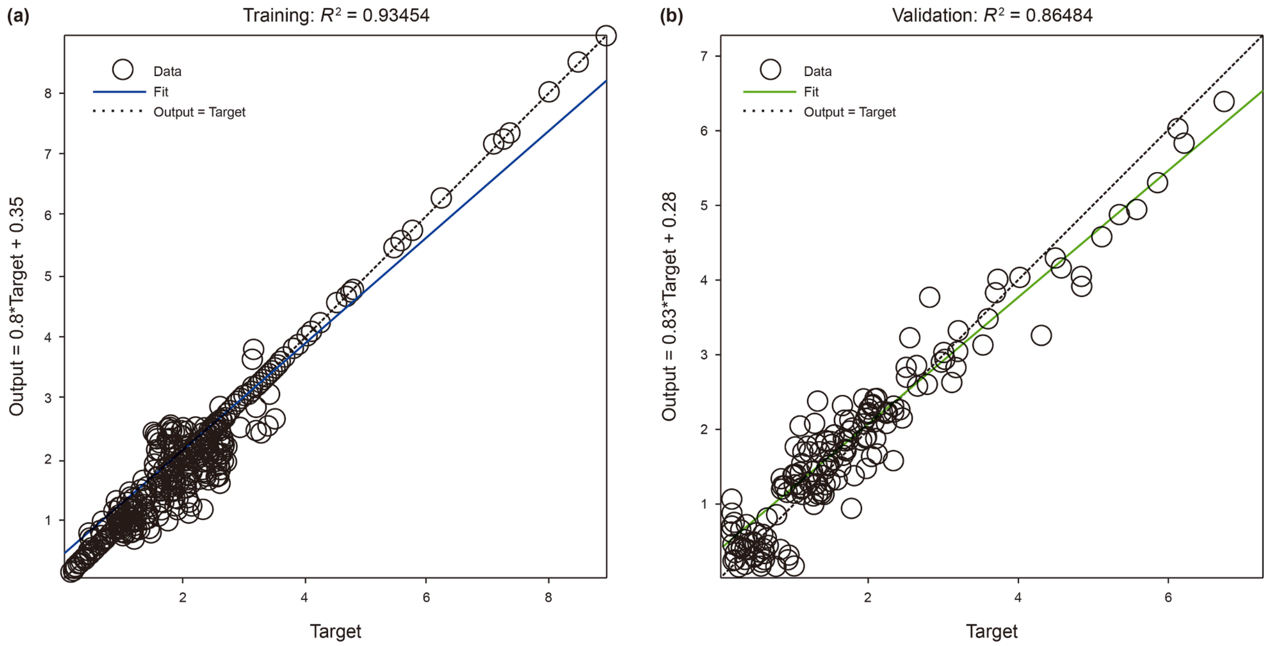

Fig. 2. XGboost training results: **(a)** training set, **(b)** validation set.

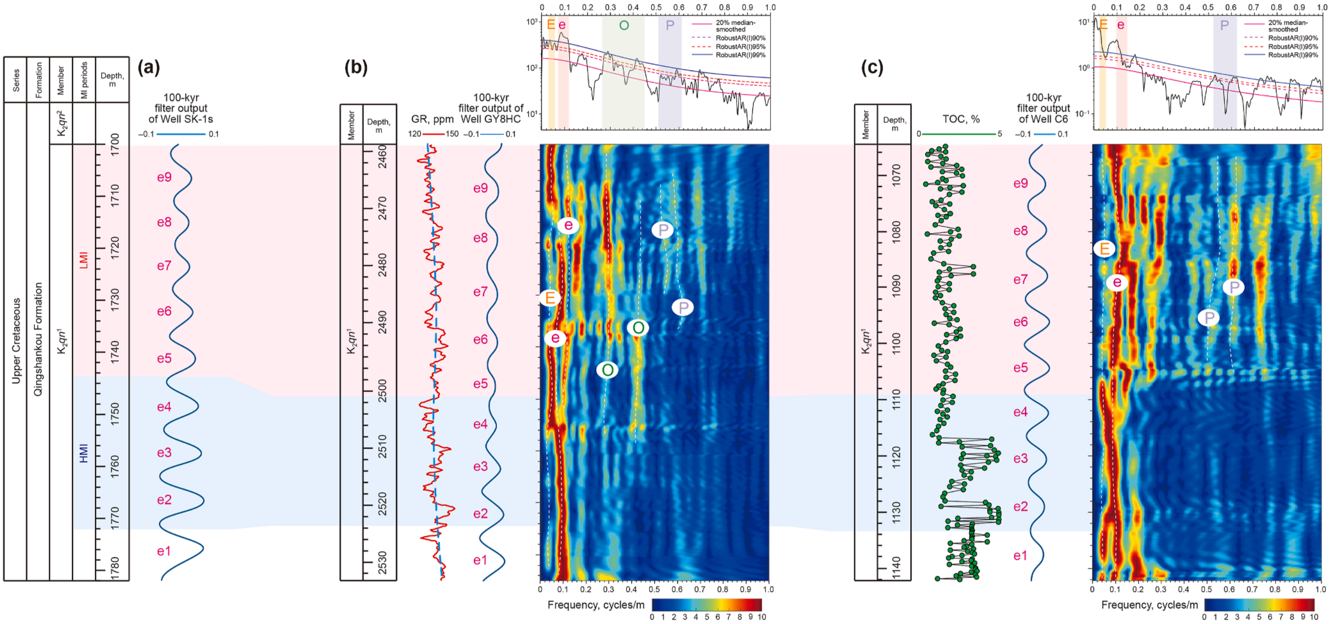

Fig. 3. Cyclostratigraphic analysis of the K_2qn^1. **(a)** Well SK-1s, data from Wu et al. (2009), **(b)** Well GY8HC, including strata of the K_2qn^1, MTM power spectra of the GR series, evolutionary power spectra, and curve of unturned GR series, ~100-kyr filters (dark blue line with passbands of 0.12 cycles/m), **(c)** Well C6, including strata of the K_2qn^1, MTM power spectra of the GR series, evolutionary power spectra, and curve of TOC, ~100-kyr filters (dark blue line with passbands of 0.13 cycles/m). E: long eccentricity; e: short eccentricity; O: obliquity; P: precession.

OCSAR of the study area increased from 0.43 × 10^{-2} GtC/(Myr·km^2) during LMI to 0.55 × 10^{-2} GtC/(Myr·km^2) during HMI. Spatial analysis within a polygon-based framework revealed substantial heterogeneity in areal OCSAR (Fig. 4(b) and (c)), ranging from 0.14 × 10^{-2} GtC/(Myr·km^2) to 1.25 × 10^{-2} GtC/(Myr·km^2) for LMI and 0.21 × 10^{-2} to 1.80 × 10^{-2} GtC/(Myr·km^2) for HMI. Quantification of the ΔOCSAR and the growth rate of areal OCSAR resolved spatially differential responses (Fig. 4(d) and (e)). These exhibited ranges of −0.12 × 10^{-2} GtC/(Myr·km^2) to 0.85 × 10^{-2} GtC/(Myr·km^2) and −26.3% to 252%, respectively. To delineate regions with distinct growth patterns, we applied a spatial clustering approach based on breaks in growth rate values, using a predefined threshold of 42% to aggregate contiguous polygons with similar growth characteristics into four coherent spatial units (Zones I–IV). This classification not only highlights regional disparities but also underscores underlying structural trends in the study area (Fig. 4(e)).

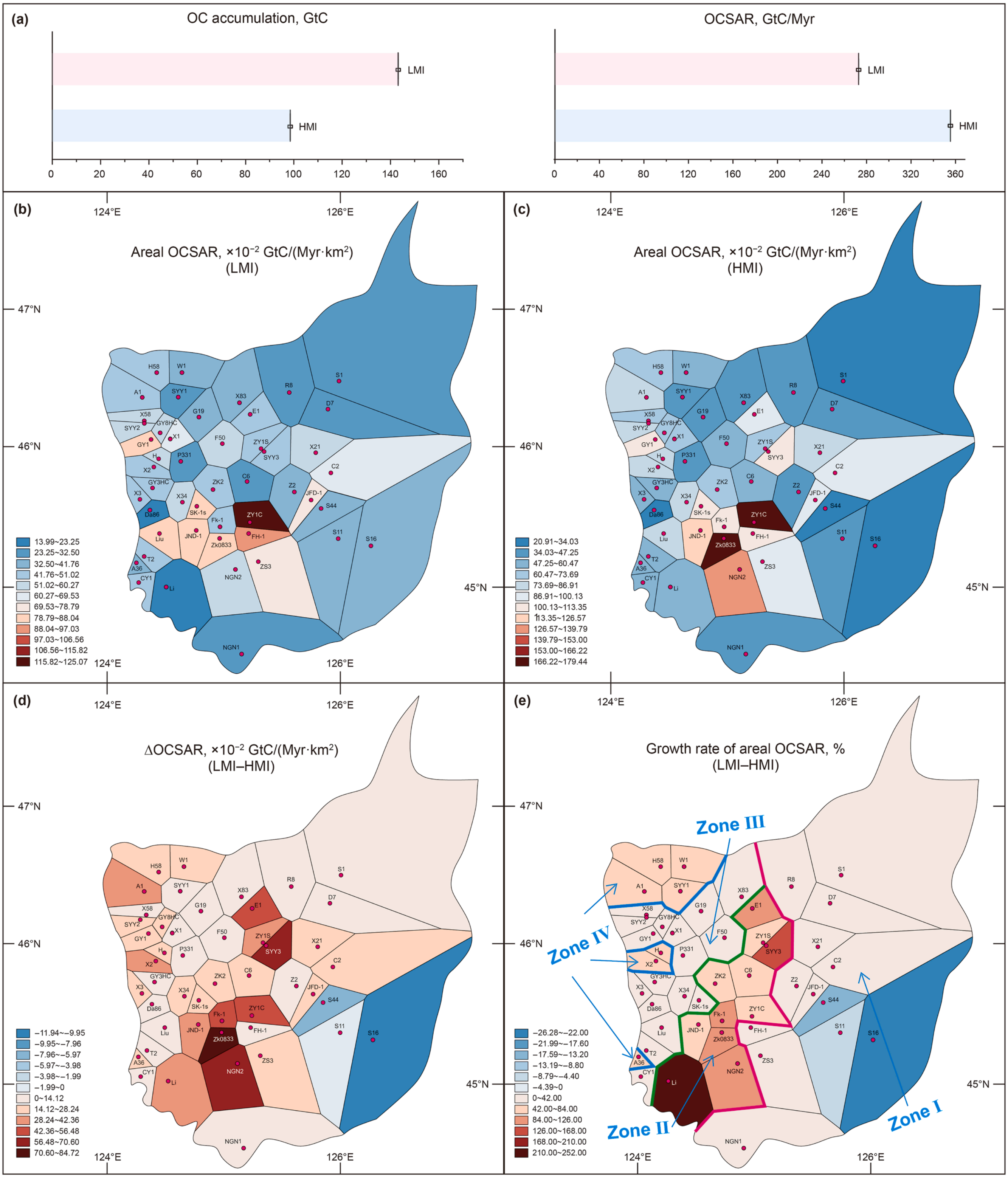

Fig. 4. **(a)** Comparison of the total OC accumulation and OCSAR during the HMI and LMI in the K_2qn^1, **(b)** areal OCSAR during the LMI, **(c)** areal OCSAR during the HMI, **(d)** absolute change in areal ΔOCSAR of polygons, (e) growth rate of areal OCSAR of polygons.

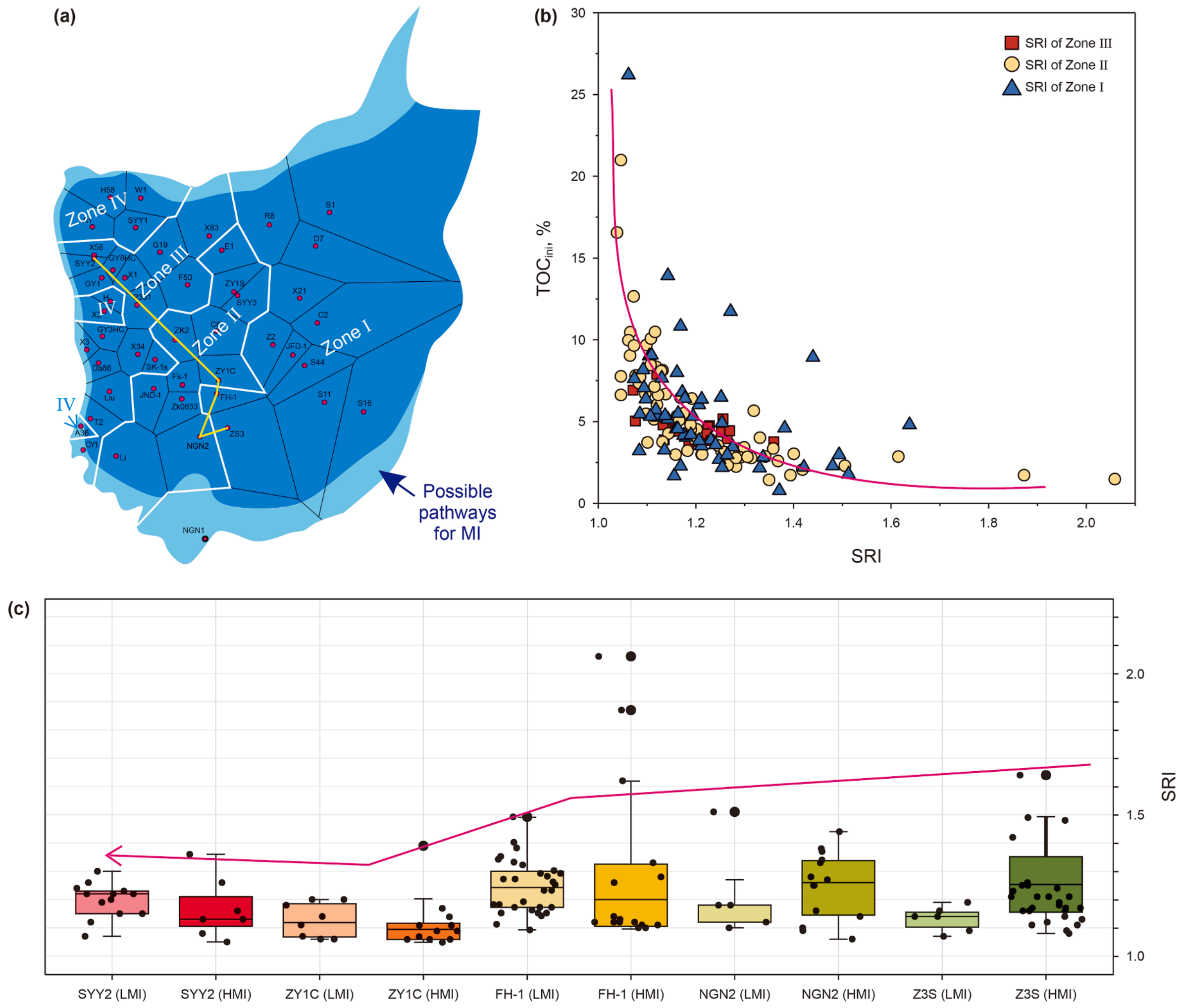

Fig. 5. **(a)** Study area and well locations, **(b)** relationships between SRI intensity and TOC$_{ini}$, **(c)** SRI intensity values for HMI versus LMI.

5. Discussion

5.1. Causes of variability in OCSAR zones

The spatial delineation of four distinct zones (I–IV) indicates that MI processes exerted multi-tiered controls on growth rates of areal OCSAR within the mega-paleolake system. These processes drove macroscopic spatial variations in growth rates of areal OCSAR across the four zones, highlighting a dynamic feedback between seawater influx and the lacustrine sedimentary environment.

Under anoxic conditions, bacterial sulfate reduction (BSR)—primarily mediated by sulfate-reducing bacteria (SRB)—utilizes sulfate (SO_4^{2-}) as an electron acceptor to accelerate OM remineralization (Fig. 5(b)). Critically, this anaerobic respiration process releases bioavailable P and trace metals (Liu et al., 2021), potentially fueling photic zone productivity during HMI and contributing to long-term atmospheric CO2 sequestration. The intensity of BSR is quantified using the sulfate reduction index (SRI), calculated as:

$$\mathrm{SRI} = (\mathrm{TOC_{ini}} + \mathrm{TS}/1.33)/\mathrm{TOC_{ini}} \tag{9}$$

where TS represents total sulfur. SRI analysis reveals a significant increase in values during the HMI at wells in Zones I and II (ZS3, NGN2, FH-1), whereas Well ZY1C exhibits a marked decrease, attributed to a paleouplift in the central basin (Zhang et al., 2022). The paleouplift impeded deep water circulation in this area, restricting the influx of seawater-derived chemical and biological components and thus suppressing BSR processes. In contrast, regions within Zones III and IV (e.g., Well SYY2) experienced comparatively weaker BSR influence during both HMI and LMI periods, as indicated by limited variability in their SRI values. SRI values at Well SYY2 are higher than those at Well ZY1C, a disparity that may be subtly influenced by volcanic activity along the western continental margin (Liu et al., 2025). Overall, BSR intensity shows a systematic attenuation, with a pronounced decline over the identified paleouplift (Fig. 5(c)).

Tang et al. (2025) integrated multiple paleoenvironmental proxies from the K_2qn^1—regarding paleoclimate, paleosalinity, paleoredox conditions, primary productivity, and OM sources—-with a XGBoost model and SHAP (Shapley Additive exPlanations) analysis. Their results demonstrate that enhanced primary productivity is the principal driver of OC accumulation during MI, followed by intensified paleoredox conditions. We conducted a multi-well correlation analysis of key paleoenvironmental proxies (e.g., productivity proxies Cu and P; redox proxies V/Cr and U; chemical index of alteration (CIA)), rigorously evaluating them within a 95% confidence interval (Fig. 6, Table S3 in Supporting Information S1). By systematically evaluating their correlations with TOC and spatial distribution patterns, we reveal synergistic

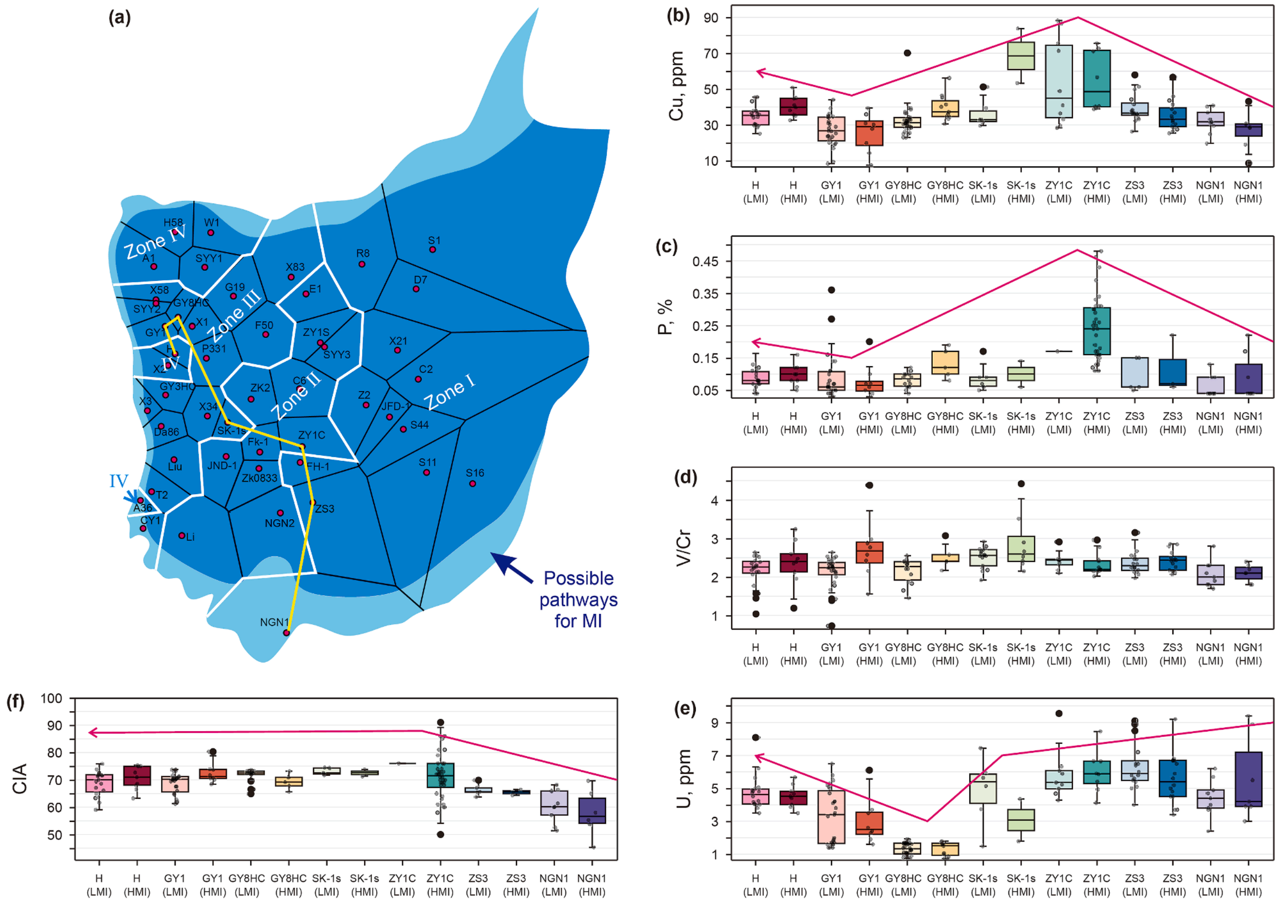

Fig. 6. **(a)** Study area and well locations, **(b)** Cu values for HMI versus LMI, **(c)** P values for HMI versus LMI, **(d)** V/Cr values for HMI versus LMI, **(e)** U values for HMI versus LMI, **(f)** CIA values for HMI versus LMI.

evolutionary relationships among key paleoenvironmental proxies.

P and Cu serve as key proxies for primary productivity, reflecting biological metabolic processes (Correll, 1998; Morel et al., 2003), with Cu being particularly indicative of productivity in the photic zone (Morel et al., 2003). Spatial analysis across Zones I to IV shows that both P and Cu exhibit a unimodal trend, initially rising, then declining, and subsequently recovering, peaking in Zone II (Fig. 6(b) and (c)). This pattern aligns closely with growth rate of areal OCSAR (Fig. 4(e)), highlighting the coupling between nutrient availability and primary productivity. In Zone I, the strongest BSR suppressed primary productivity, resulting in lower Cu values during HMI compared to LMI. This trend reversed in Zone II, where BSR began to weaken, and the release of nutrients by SRB significantly elevated Cu levels during the HMI. Although BSR intensity and Cu concentrations further declined in Zones III and IV, Cu levels remained slightly higher in the HMI (Fig. 6(b)). In contrast, P distribution lacks consistent spatial regularity, underscoring the critical role of seawater in modulating biogeochemical cycles in the epilimnion. Paleoredox proxies display distinct behaviors: V/Cr ratios remain spatially stable (mostly 2–3; Fig. 6(d)), indicating persistent anoxic in the deep lake. Conversely, U content, which is a more sensitive proxy for redox conditions, exhibits a nonlinear trend, with reducing conditions weakening from Zones I to III but rebounding sharply in Zone IV (Fig. 6(e)). We interpret this pattern as follows: the strongest OM remineralization in Zone I likely consumed dissolved oxygen, enhancing reducing conditions. Subsequent decline in BSR led to weaker reducing conditions in Zones II and III. The marked resurgence of reducing conditions in Zone IV is likely driven by sustained terrigenous OM input, because terrigenous OM consumes dissolved oxygen in water bodies, leading to hypoxia. The CIA, serving as a terrigenous chemical weathering proxy, is significantly higher in Zone IV than in Zones I and II, supporting this viewpoint (Fig. 6(f)). We propose that intense terrigenous OM inputs induced a metalimnetic oxygen minimum (MOM) phenomenon along lake margins (Bian et al., 2025), where elevated oxygen consumption near source areas formed localized anoxic zones.

5.2. OC accumulation models during the HMI and LMI

The K_2qn^1 was deposited under predominantly anoxic conditions. Massive inputs of SRB and SO42- into the paleolake occurred, while bacterially mediated OM remineralization further enhanced nutrient availability and stimulated primary productivity. In Zone I, the strongest BSR significantly suppressed primary productivity and strengthened OM remineralization. Consequently, the OC accumulation efficiency was markedly reduced, as evidenced by data from Wells S11, S16, and S44 (Fig. 4(e)). This resulted in a NE-trending belt characterized by negative or minimal growth rates of areal OCSAR. In Zone II, paleouplift triggered a sharp decrease in the SRI, which led to a significant enhancement of photic zone productivity coupled with strongly reducing conditions. This combination produced the highest growth rates of areal OCSAR, with accumulation efficiency increasing by up to

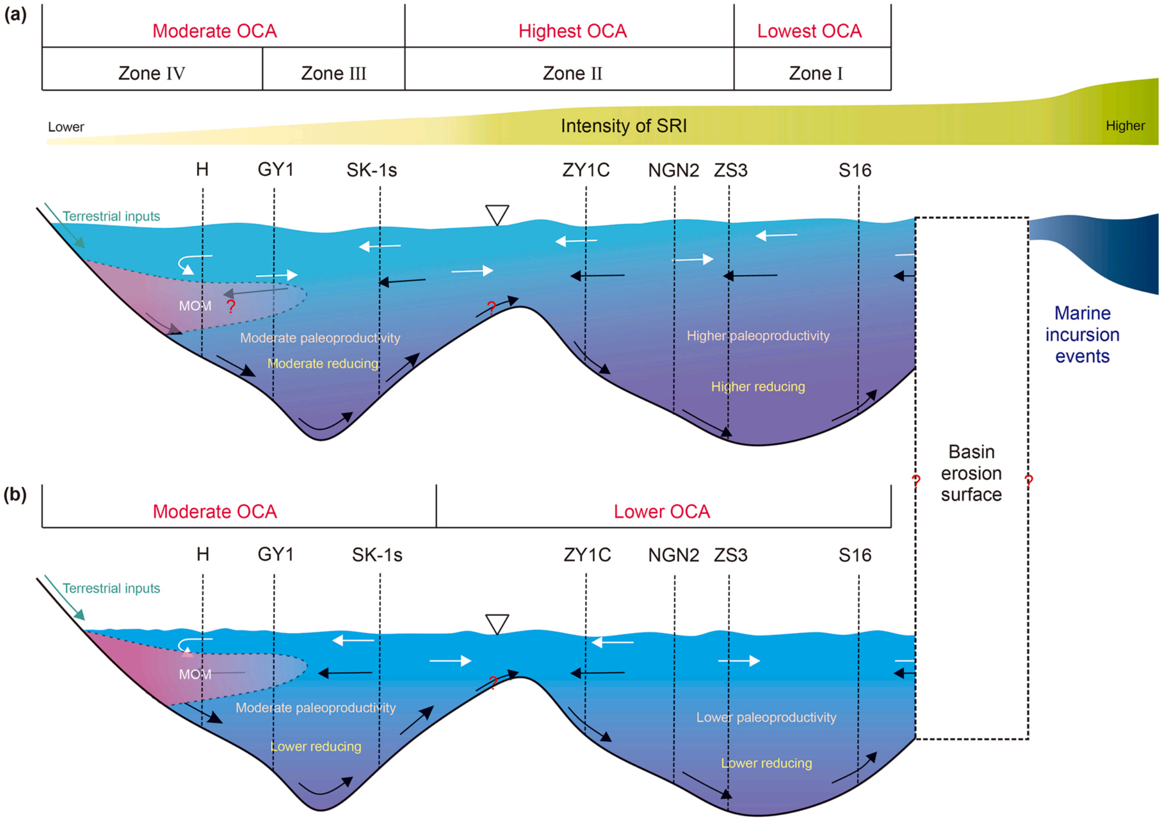

Fig. 7. Organic carbon accumulation (OCA) models in the K_2qn^1 of Songliao Basin. **(a)** HMI period, **(b)** LMI period. The directions of epilimnion water circulation and hypolimnion water circulation are shown in white and black arrows, respectively. MOM: metalimnetic oxygen minimum.

252% (Fig. 4(e)). Further in Zone III, a weakened nutrient-reduction gradient resulted in a reduced efficiency gain of approximately 20% (Fig. 4(e)). In Zone IV, a rebound in OC accumulation efficiency occurred, likely driven by sustained terrigenous OM input. The MOM associations enhanced OC accumulation, enabling Zone IV to maintain higher growth rates of areal OCSAR despite lower primary productivity. Although MI may have suppressed terrigenous inputs and potentially attenuated MOM reactivity, the OC accumulation efficiency in this zone was documented to have increased. Overall, HMI during the K_2qn^1 in the Songliao Basin generated a distinct four-stage oscillatory growth pattern in OC accumulation efficiency (Fig. 7(a)(b)).

Although integrated basin-scale calculations indicate a 28.8% increase in OCSAR during HMI intervals, the spatial distribution of negative-growth zones reveals that both basin geometry and seawater influxes fundamentally modulated the OC accumulation response of the paleolake. Notably, Late Cretaceous tectonic inversion during the Nenjiang Formation triggered extensive erosion of K_2qn (Feng et al., 2010), suggesting that larger theoretical negative-growth zones may have systematically inflated this OCSAR. Recent source-to-sink analyses indicate that eroded areas during K_2qn likely represented <50% of the preserved depositional areas (Li et al., 2025). Furthermore, studies of the MI of the Nenjiang Formation demonstrate that seawater contributed <5% of total lake volume (Qin et al., 2024)—a characteristic potentially applicable to K_2qn^1 given comparable hydrographic conditions. Emerging research additionally suggests that episodic MI could have driven localized accumulation increases substantially exceeding basin-wide averages (Ma et al., 2025). In summary, while MI demonstrably enhanced the OC accumulation capacity of the Songliao Basin, the reported 28.8% net growth rate represents a provisional estimate. Due to current data constraints (regarding the estimation of TOC_{ini}), errors inherent to machine learning methods (particularly evident scatter within the low-TOC range), and limited progress in related research, this value may deviate from paleoenvironmental realities. Nonetheless, despite potential biases, the model-indicated upward trend of areal OCSAR growth rates from the HMI to LMI, as well as its four-zone spatial heterogeneity pattern are considered robust, because they are primarily based on the correlation of temporal OCSAR changes within individual wells. With the publication of new research and data, the model presented in this study will be further validated and refined in the future.

5.3. Validation case of OC accumulation models

To validate the general applicability of the OC accumulation models established for HMI and LMI intervals, we selected Member 1 (K_2n^1) and Member 2 (K_2n^2) of the Nenjiang Formation (K_2n) in the Songliao Basin as a case study. The K_2n, belonging to the Upper Cretaceous strata, is situated between the Yaojia and Sifangtai formations (Wang et al., 2013). It is subdivided from bottom to top into members 1 to 5. Among these, the K_2n^1 and K_2n^2 are characterized by large-scale lacustrine sediments. In contrast, during the depositional period of Members 3 to 5, the sedimentary facies shifted to delta–lacustrine sediments (Fig. 8(a); Liu et al., 2023a). This study focuses on the K_2n^1 and K_2n^2 for validation, primarily for the following reasons: (i) the K_2n^1 and lower K_2n^2 record clear multiphase MI, reliably evidenced by positive excursions in pyrite sulfur isotopes, characteristic biomarker profiles, and the presence of marine-derived foraminifers and calcareous nannofossils (Hu et al., 2015; Xi et al., 2016; Cao et al., 2019); (ii) the Songliao Basin was in a widespread thermal subsidence stage during the K_2n^1 and K_2n^2, particularly

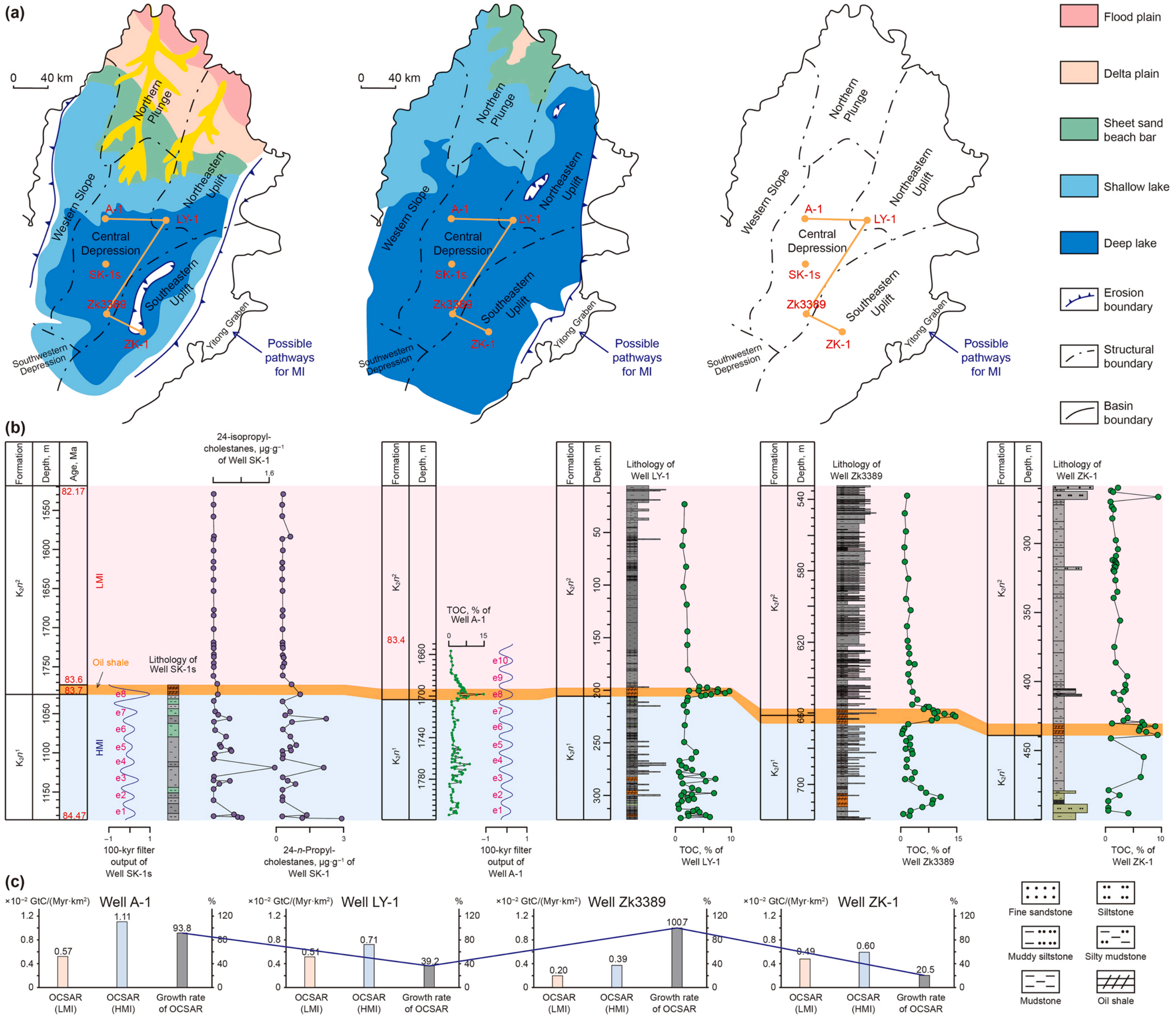

Fig. 8. OC accumulation characteristics in Member 1 (K_2n^1) and Member 2 (K_2n^2) of the Nenjiang Formation in the Songliao Basin. **(a)** Depositional systems of the K_2n^1 and K_2n^2 (Feng et al., 2010) and location of five wells, **(b)** paleoenvironmental proxies during HMI and LMI, date from Bechtel et al. (2012), Wu et al. (2014), Hu et al. (2015), Xu et al. (2015), Cao et al. (2019), Liu et al. (2022), **(c)** areal OCSAR during HMI and LMI and growth rates of areal OCSAR in four wells.

with a regional oil shale layer developed at the lower K_2n^2 (Niu et al., 2021). This stable tectonic setting provides an exceptionally complete and continuous sedimentary record, which is ideal for detailed interwell correlation.

Using the same methodology, we found that biomarker and geochronological analyses from Well SK-1 indicate that the HMI spanned 83.6–84.47 Ma, while the LMI spanned 82.17–83.6 Ma, which precisely coincides with the oil shale at the K_2n^2 base (Wu et al., 2014; Hu et al., 2015) (Fig. 8(b)). Owing to limited TOC data for the entire K_2n^1 and K_2n^2, we selected four wells—ZK-1, Zk3389, LY-1, and A-1 (Table S2 in Supporting Information S1)—for further analysis. The oil shale at the base of K_2n^2 serves as a marker bed that can be correlated across the entire basin. Thus, the boundaries between HMI and LMI in the four wells were defined by the top depth of the oil shale. For Well A-1, which lacks TOC in the upper K_2n^2, we employed a time-series analysis of TOC. This was integrated with an interwell ATS using the 100-kyr curve from Well SK-1s to refine the chronological framework. The results demonstrate that the top TOC depth in Well A-1 corresponds to 83.4 Ma (Fig. 8(b)). Subsequently, we calculated the areal OCSAR and growth rates of areal OCSAR for both HMI and LMI intervals. Notably, as these calculations are derived from a single well, the H_{Xd} in formula (4) equals H_X, and S_X is set to 1.

Growth rates of areal OCSAR in wells ZK-1, ZK3389, LY-1, and A-1 exhibit trends consistent with those observed in the K_2qn^1 (Fig. 8(c)), supporting the robustness of our previously established models. Two aspects require further discussion: (i) compared to the underlying K_2n^1, the K_2n^2 experienced further lake expansion, resulting in more stable sedimentary conditions. This stability is reflected in relatively uniform TOC values across other wells (Fig. 8(c)), suggesting that missing TOC data in Well A-1 likely has a limited impact on growth rates of areal OCSAR; (ii) Negative areal OCSAR growth rates—as seen in the K_2qn^1—were not identified in the K_2n^1 and K_2n^2, possibly due to more intense erosion during the tectonic inversion phase (Li et al., 2021) or a lack of TOC data from wells in the basin margins. Nevertheless, the significantly lower value in ZK-1 (20.5%) compared to the other wells suggests suppressed OC accumulation under MI conditions (Fig. 8(c)).

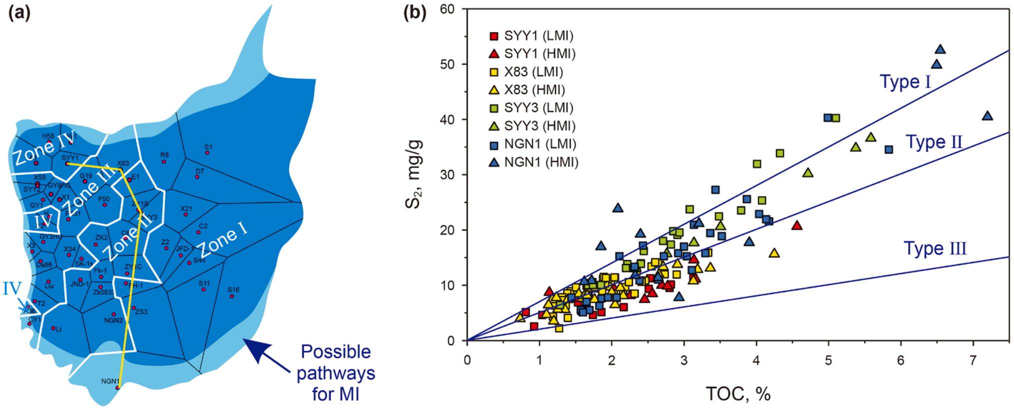

Fig. 9. **(a)** Study area and well locations, **(b)** Correlation between S_2 and TOC content.

5.4. Implication for the OC sink dynamic and exploration of lacustrine shale oil and gas

Quantification confirms that rapid increases in OCSAR during HMI intervals were amplified by episodic seawater influxes. Crucially, this reveals a spatially heterogeneous response mechanism modulated by biogeochemical gradients, a pattern likely applicable to lacustrine systems globally. This implies that carbon flux estimates derived from localized records lack broad applicability. This demonstrates that biological activity and basin morphology exert primary controls on nutrient distribution and water-column chemistry, thereby helping to resolve long-standing debates regarding the net impacts of MI.

For lacustrine shale oil and gas exploration, TOC content and kerogen type constitute key sweet-spot indicators (Lv et al., 2025b), directly guiding target selection. Our modeling demonstrates that the HMI enhanced nutrient recycling and preservation conditions, significantly elevating OM accumulation in Zone IV (Gulong Sag, and southern Qijia Sag) and Zone II (northern Changling Sag, and the southwestern Southeastern Uplift around a paleouplift). These areas represent priority targets for shale hydrocarbon exploration. During the LMI, the relationship between S_2 and TOC (Fig. 9(b)) indicates that Zones II and III are dominated by Type I kerogen, primarily derived from planktonic algae (Table S3 in Supporting Information S1). In contrast, Zone IV exhibits a higher abundance of Type III kerogen, suggesting a stronger contribution from terrestrial higher plants. During the HMI, the kerogen composition in all zones shifts towards a predominance of Type II kerogen (primarily derived from marine plankton). Notably, Zone I, due to its proximity to the MI pathways, consistently shows a higher proportion of Type II kerogen throughout both intervals, reflecting its persistent depositional connection to MI. Based on the established geological characteristics, we propose an integrated geology-engineering development strategy for shale oil and gas. For the LMI intervals of Zone II and III (dominated by Type I kerogen), we recommend prioritizing the deployment of high-productivity oil wells to unlock their maximum flow potential (Liang et al., 2025). In contrast, Zone I and the HMI intervals of Zone II to IV (primarily Type II kerogen) require customized fracturing parameters aligned with organic maturity gradients (Hui et al., 2024). Meanwhile, the LMI intervals of Zone IV warrant a focused approach toward shale gas exploitation. This approach—precisely aligning geological characteristics with engineering design—is essential for efficiently converting geologic resources into economically recoverable reserves.

6. Conclusions

Integrating high-resolution geological records from the K_2qn^1 in the Songliao Basin with multi-proxy analysis and machine learning-assisted TOC prediction, this study quantitatively demonstrates that the HMI significantly enhanced OC accumulation within a mega-paleolake system. Our calculations reveal that both total OC accumulation and areal OCSAR during the HMI markedly exceeded those during the LMI. Specifically, the OCSAR increased from 276.9 GtC/Myr to 356.8 GtC/Myr, while the areal OCSAR of the study area rose from 0.43×10^{-2} GtC/(Myr·km^2) to 0.55×10^{-2} GtC/(Myr·km^2). Critically, this enhancement was not spatially uniform. The interplay of seawater influxes, basin morphology, and terrigenous inputs created a complex biogeochemical gradient, modulating BSR, redox conditions, and nutrient availability. This resulted in pronounced spatial heterogeneity, defining four distinct zones (I–IV) with growth rates of areal OCSAR ranging from −26.3% to 252%. This spatial pattern reveals a dynamic feedback mechanism: the net effect of MI on OC accumulation is ultimately determined by the balance between enhanced primary productivity fueled by nutrient inputs and OM remineralization driven by BSR. The robustness and broader applicability of our four-zone conceptual models are confirmed through cross-validation with the independent MI sequences of the K_2n^1 and K_2n^2, which exhibit consistent trends in OC accumulation dynamics. Our findings establish MI as a key geological process capable of significantly enhancing the carbon sequestration capacity of mega-paleolakes. Furthermore, the identified heterogeneity in OC accumulation, particularly the high potential of Zones II and IV during HMI, along with the associated shifts in kerogen type, provides a critical geological framework for optimizing sweet-spot prediction and exploitation strategies for lacustrine shale hydrocarbons within MI sequences globally.

CRediT authorship contribution statement

Ke-Rui Wu: Writing – review & editing, Writing – original draft, Software, Methodology, Data curation, Conceptualization. **Yu Sun:** Writing – review & editing, Funding acquisition. **Da-Ming Yang:** Writing – review & editing, Writing – original draft, Methodology, Formal analysis. **Fu-Li Fang:** Visualization, Software. **Bai-Quan Yan:** Writing – review & editing. **Jie Zhou:** Visualization, Data curation. **Tao Yu:** Visualization, Data curation.

Declaration of competing interest

The authors declare that they have no known competing financial interests or personal relationships that could have appeared to influence the work reported in this paper.

Acknowledgements

This research was supported by the Heilongjiang Provincial Key Research and Development Program (No. JD24C001). We appreciate the careful reviews and constructive suggestions from the four reviewers and journal editors. We are also grateful to Dr. Peng-Fei Ma from Tongji University for his advice on data processing.

Supplementary data

Supplementary data to this article can be found online at https://doi.org/10.1016/j.petsci.2026.03.033.

References

Allen, D.T., Torres, V.M., Thomas, J., Sullivan, D.W., Harrison, M., Hendler, A., Herndon, S.C., Kolb, C.E., Fraser, M.P., Hill, A.D., Lamb, B.K., Miskimins, J., Sawyer, R.F., Seinfeld, J.H., 2013. Measurements of methane emissions at natural gas production sites in the United States. Proc. Natl. Acad. Sci. USA 110, 17768–17773. https://10.1073/pnas.1304880110.

Bechtel, A., Jia, J., Strobl, S.A.I., Sachsenhofer, R.F., Liu, Z., Gratzer, R., Püttmann, W., 2012. Palaeoenvironmental conditions during deposition of the Upper Cretaceous oil shale sequences in the Songliao Basin (NE China): Implications from geochemical analysis. Org. Geochem. 46, 76–95. https://doi.org/10.1016/j.orggeochem.2012.02.003.

Bian, L., Wang, X., Chappaz, A., Xiong, Z., Ye, M., Zhang, S., Zhao, W., 2025. Elemental-organic geochemical evidence for the lacustrine metalimnetic oxygen minimum dynamics in the Mid-Late Triassic Chang 7 shales. Earth Planet Sci. Lett. 651, 119153. https://10.1016/j.epsl.2024.119153.

Byrum, S., Lieberman, B.S., 2021. Phylogeny and biogeography of some Cretaceous spatangoid echinoids with special emphasis on taxa from the Western Interior Seaway. J. Paleontol. 95, 613–623. https://10.1017/jpa.2020.102.

Cao, H., Kaufman, A.J., Shan, X., 2019. Coupled isotopic evidence for elevated pCO_2 and nitrogen limitation across the Santonian–Campanian transition. Chem. Geol. 504, 136–150. https://doi.org/10.1016/j.chemgeo.2018.11.006.

Chen, R.Q., Bai, X., Huang, C.Z., Wu, X., Shang, F., 2024. How marine incursions affect the sedimentary environment and the quality of source rocks in the Upper Cretaceous Songliao Basin, NE China. Mar. Petrol. Geol. 170. https://10.1016/j.marpetgeo.2024.107140.

Chen, T., Guestrin, C., 2016. XGBoost: A scalable tree boosting system. In: Proceedings of the 22nd ACM SIGKDD International Conference on Knowledge Discovery and Data Mining. Association for Computing Machinery, San Francisco, California, USA, pp. 785–794. https://doi.org/10.1145/2939672.2939785.

Cleveland, W.S., 1979. Robust locally weighted regression and smoothing scatterplots. J. Am. Stat. Assoc. 74 (368), 829–836. https://doi.org/10.1080/01621459.1979.10481038.

Correll, D.L., 1998. The role of phosphorus in the eutrophication of receiving waters: A review. J. Environ. Qual. 27, 261–266. https://doi.org/10.2134/jeq1998.00472425002700020004x.

Ding, X., Qian, L., Jiang, W., Liu, H., Yiming, A., Zha, M., Qu, J., Jiang, Z., 2024. Review of bacterial sulfate reduction in lacustrine deposition and its identification in the Jimsar Sag, Junggar Basin. Mar. Petrol. Geol. 163, 106801. https://doi.org/10.1016/j.marpetgeo.2024.106801.

Feng, Z.Q., Jia, C.Z., Xie, X.N., Zhang, S., Feng, Z.H., Cross, T.A., 2010. Tectonostratigraphic units and stratigraphic sequences of the nonmarine Songliao basin, northeast China. Basin Res. 22, 79–95. https://10.1111/j.1365-2117.2009.00445.x.

Gao, J., Jin, Z., Liang, X., 2025. Lacustrine organic carbon sequestration driven by volcanism: A case study of the third submember of the Chang 7 Member of the Yanchang Formation in the Ordos Basin. Pet. Sci. https://doi.org/10.1016/j.petsci.2025.05.015.

Hackley, P.C., Cardott, B.J., 2016. Application of organic petrography in North American shale petroleum systems: A review. Int. J. Coal Geol. 163, 8–51. https://10.1016/j.coal.2016.06.010.

Han, G., Wang, J.Y., Zhang, W.J., Huang, Q.H., 2011. Organic geochemical stratum characteristics from Member l of Qingshankou Formation in the Well Mao 206 of Songliao Basin. Sci. Technol. Eng. 11 (15), 3393–3397.

Hou, D., Li, M., Huang, Q., 2000. Marine transgressional events in the gigantic freshwater lake Songliao: Paleontological and geochemical evidence. Org. Geochem. 31, 763–768. https://doi.org/10.1016/S0146-6380(00)00065-6.

Hu, J.F., Peng, P.A., Liu, M.Y., Xi, D.P., Song, J.Z., Wan, X.Q., Wang, C.S., 2015. Seawater incursion events in a Cretaceous Paleo-lake revealed by specific marine biological markers. Sci. Rep. 5, 9508. http://10.1038/srep09508.

Hu, T., Pang, X., Jiang, F., Wang, Q., Liu, X., Wang, Z., Jiang, S., Wu, G., Li, C., Xu, T., Li, M., Yu, J., Zhang, C., 2021. Movable oil content evaluation of lacustrine organic-rich shales: Methods and a novel quantitative evaluation model. Earth Sci. Rev. 214, 103545. https://doi.org/10.1016/j.earscirev.2021.103545.

Huang, H., Gao, Y., Ma, C., Jones, M.M., Zeeden, C., Ibarra, D.E., Wu, H., Wang, C., 2021. Organic carbon burial is paced by a ~173-ka obliquity cycle in the middle to high latitudes. Sci. Adv. 7, eabf9489. https://doi.org/10.1126/sciadv.abf9489.

Huang, Y.J., Yang, G.S., Gu, J., Wang, P.K., Huang, Q.H., Feng, Z.H., Feng, L.J., 2013. Marine incursion events in the Late Cretaceous Songliao Basin: Constraints from sulfur geochemistry records. Palaeogeogr. Palaeoclimatol. Palaeoecol. 385, 152–161. https://10.1016/j.palaeo.2013.03.017.

Hui, S.S., Pang, X.Q., Jiang, F.J., Wang, C.X., Mei, S.X., Hu, T., Pang, H., Li, M., Zhou, X.L., Shi, K.Y., 2024. Quantitative effect of kerogen type on the hydrocarbon generation potential of Paleogene lacustrine source rocks, Liaohe Western Depression, China. Pet. Sci. 21, 14–30. https://doi.org/10.1016/j.petsci.2023.09.004.

Jones, M.M., Ibarra, D.E., Gao, Y., Sageman, B.B., Selby, D., Chamberlain, C.P., Graham, S.A., 2018. Evaluating Late Cretaceous OAEs and the influence of marine incursions on organic carbon burial in an expansive East Asian paleolake. Earth Planet Sci. Lett. 484, 41–52. https://10.1016/j.epsl.2017.11.046.

Lai, J., Zhao, F., Xia, Z., Su, Y., Zhang, C., Tian, Y., Wang, G., Qin, Z., 2024. Well log prediction of total organic carbon: A comprehensive review. Earth Sci. Rev. 258, 104913. https://doi.org/10.1016/j.earscirev.2024.104913.

Laskar, J., Fienga, A., Gastineau, M., Manche, H., 2011. La2010: A new orbital solution for the long-term motion of the Earth. Astron. Astrophys. 532, A89. https://10.1051/0004-6361/201116836.

Li, M., Hinnov, L., Kump, L., 2019. Acycle: Time-series analysis software for paleoclimate research and education. Comput. Geosci. 127, 12–22. https://10.1016/j.cageo.2019.02.011.

Li, P., Liu, Z.B., Bi, H., Jiang, T., Bian, R.K., Wang, P.W., Shang, X.Y., 2024. Differences in and factors controlling organic matter enrichment in the Ziliujing Formation shale in the Sichuan Basin. Pet. Sci. 21, 77–86. https://10.1016/j.petsci.2023.10.020.

Li, P., Zhang, F.Q., Dilek, Y., Sun, D.H., Huang, J.L., Zhu, K.Y., Lin, X.B., Cheng, X.G., Chen, H.L., 2025. Spatial–temporal evolution of the source-to-sink system in the early and mid-cretaceous Songliao Basin, Northeast China, and its constraints on basin prototype boundaries and paleogeography. Palaeogeogr. Palaeoclimatol. Palaeoecol. 663, 112762. https://10.1016/j.palaeo.2025.112762.

Li, Z.Q., Chen, J.L., Zou, H., Wang, C.S., Meng, Q.A., Liu, H.L., Wang, S.Z., 2021. Mesozoic–Cenozoic tectonic evolution and dynamics of the Songliao Basin, NE Asia: Implications for the closure of the Paleo-Asian Ocean and Mongol-Okhotsk Ocean and subduction of the Paleo-Pacific Ocean. Earth Sci. Rev. 218, 103471. https://10.1016/j.earscirev.2020.103471.

Liang, T., Zou, Y.R., Zhan, Z.W., Peng, P.A., 2025. Study on swelling and retention of liquid hydrocarbon compounds by type I kerogen. Pet. Sci. 22, 3960–3966. https://doi.org/10.1016/j.petsci.2025.07.013.

Liu, B., Liu, L.B., Fu, J., Lin, T.F., He, J.L., Liu, X.Z., Liu, Y.C., Fu, X.F., 2023a. The songliao super Basin in northeastern China. AAPG Bull. 107, 1257–1297. https://10.1306/02242321181.

Liu, L.J., Li, J.H., Fu, X.L., Bai, Y., Zheng, Q., 2025. Characteristics and geological significance of volcanic ash of Cretaceous Qingshankou formation in the central depression of northern Songliao Basin. Lithologic reservoirs 37 (5), 145–154. https://doi.org/10.12108/yxyqc.20250513.

Liu, Q.Y., Li, P., Jin, Z.J., Liang, X.P., Zhu, D.Y., Wu, X.Q., Meng, Q.Q., Liu, J.Y., Fu, Q., Zhao, J.H., 2021. Preservation of organic matter in shale linked to bacterial sulfate reduction (BSR) and volcanic activity under marine and lacustrine depositional environments. Mar. Petrol. Geol. 127, 104950, 127. https://10.1016/j.marpetgeo.2021.104950.

Liu, W., Liu, M., Yang, T., Liu, X., Them, T.R., Wang, K., Bian, C., Meng, Q.a., Li, Y., Zeng, X., Zhao, W., 2022. Organic matter accumulations in the Santonian–Campanian (Upper Cretaceous) lacustrine Nenjiang shale (K2n) in the Songliao Basin, NE China: Terrestrial responses to OAE3? Int. J. Coal Geol. 260, 104069. https://doi.org/10.1016/j.coal.2022.104069.

Liu, W.G., Li, X.Z., An, Z.S., Xu, L.M., Zhang, Q.L., 2013. Total organic carbon isotopes: A novel proxy of lake level from Lake Qinghai in the Qinghai–Tibet Plateau, China. Chem. Geol. 347, 153–160. https://10.1016/j.chemgeo.2013.04.009.

Liu, Y.K., Wang, H.J., Zhang, J.Y., Liu, Z.W., Chen, F.Z., Wang, X.M., Zhang, S.C., Liu, H., 2023b. Rare earth elemental and Sr isotopic evidence for seawater intrusion event of the Songliao Basin 91 million years ago. Pet. Sci. 20, 1347–1362. https://doi.org/10.1016/j.petsci.2022.11.015.

Lv, D., Wang, H.J., Li, G., Zhang, J.Y., Fu, X.L., Liu, C., Wang, X.M., Zhu, R.K., Zhang, S.C., 2023. Paleobiological evidence of the paleowater environment evolution during deposition of the Qingshankou shale in the Songliao Basin. Oil Gas Geol. 44 (4), 857–868. https://doi.org/10.11743/ogg20230405.

Lv, D., Zhao, Y., Steel, R.J., Jia, H., Raji, M., Zhang, Z., Ju, L., Gong, L., Wang, X., 2025a. Massive organic carbon burial in the North China Basin is a main contributor to peak late Paleozoic Ice Age in early Asselian. Earth Planet Sci. Lett. 661, 119370. https://doi.org/10.1016/j.epsl.2025.119370.

Lv, J.H., Hu, T., Zhang, W., Jiang, F.J., Xue, J., Zhang, C.X., Qi, Z.G., Huang, R.D., Hu, M.L., Jiang, S., 2025b. Microscopic oil occurrence in the Permian alkaline lacustrine shales: Fengcheng formation, Mahu Sag, Junggar Basin. Pet. Sci. 22, 1407–1427. https://doi.org/10.1016/j.petsci.2025.01.005.

Ma, J., Cury, L.F., Rumbelsperger, A.M.B., Albrecht, H.L., Adams, E.W., Amthor, J.E., Cui, X.Q., Crémière, A., Sato, K., Bergmann, K.D., Summons, R.E., 2025. Ecosystem changes after Early Cretaceous seawater intrusion into the proto-South Atlantic Ocean. Commun. Earth Environ. 6, 51. https://10.1038/s43247-025-02029-2.

Ma, P., Liu, Z., Jiang, M., Cheng, H., Zhang, L., Cai, D., 2022. Carbon Sequestration of the Middle Miocene Sunda Shelf Facilitated Global Climate Change. Geophys. Res. Lett 49, e2022GL100638. https://doi.org/10.1029/2022GL100638.

Morel, F.M.M., Milligan, A.J., Saito, M.A., 2003. Marine bioinorganic chemistry: The role of trace metals in the Oceanic cycles of major nutrients. Treatise on Geochemistry 6, 625. http://10.1016/b0-08-043751-6/06108-9.

Niu, L., Gao, Y., Huang, H., Tian, X., Dong, T., Yang, Q., Cao, X., Wang, C., 2021. Controlling factors for organic carbon burial in the Late Cretaceous Nenjiang Formation of the Songliao Basin, NE China. Energies 14 (16), 4783. https://doi.org/10.3390/en14164783.

Qin, Z., Liu, J., Cui, H., Konhauser, K.O., Huang, H., Xu, D., Gao, Y., Wu, H., Wang, C., 2024. Rhenium–platinum group elements reveal seawater incursion induced massive lacustrine organic carbon burial. Geochim. Cosmochim. Acta 384, 168–177. https://10.1016/j.gca.2024.09.031.

Santos, T.P., Bione, F.R.A., Venancio, I.M., Bernardes, M.C., Belem, A.L., Lisboa, L.P., Franco, D.R., Diaz, R.A., Moreira, M., Leonardo, N.F., Souza, I.V., Spigolon, A.L.D., Albuquerque, A.L.S., 2022. Late Cretaceous astrochronology, organic carbon evolution, and paleoclimate inferences for the subtropical Western South Atlantic, Espirito Santo Basin. Cretac. Res. 129, 105032. https://10.1016/j.cretres.2021.105032.

Scott, R.W., Wan, X.Q., Wang, C.S., Huang, Q.H., 2012. Late Cretaceous chronostratigraphy (Turonian–Maastrichtian): SK1 core Songliao Basin, China. Geosci. Front. 3, 357–367. https://10.1016/j.gsf.2012.02.004.

Sun, D., He, Y., Wu, J., Liu, W., Sun, Y., 2019. Hydrological and ecological controls on autochthonous carbonate deposition in lake systems: A case study from Lake Wuliangsu and the global perspective. Geophys. Res. Lett. 46, 6583–6593. https://doi.org/10.1029/2019GL082224.

Tang, B., Meng, Q., Hu, F., Jiang, N., Yang, L., Xing, J., Liu, Z., Zhang, Y., 2025. Effect of Late Cretaceous marine incursions on lacustrine organic carbon burial in East Asia: Perspectives from machine learning and geochemistry. Palaeogeogr. Palaeoclimatol. Palaeoecol. 679, 113304. https://doi.org/10.1016/j.palaeo.2025.113304.

Thomson, D.J., 1982. Spectrum estimation and harmonic-analysis. Proc. IEEE 70, 1055–1096. In: https://10.1109/proc.1982.12433.

Wang, C., Scott, R.W., Wan, X., Graham, S.A., Huang, Y., Wang, P., Wu, H., Dean, W.E., Zhang, L., 2013. Late Cretaceous climate changes recorded in Eastern Asian lacustrine deposits and North American Epieric sea strata. Earth Sci. Rev. 126, 275–299. https://doi.org/10.1016/j.earscirev.2013.08.016.

Wu, H., Hinnov, L.A., Zhang, S., Jiang, G., Yang, T., Li, H., Xi, D., Ma, X., Wang, C., 2022. Continental geological evidence for Solar System chaotic behavior in the Late Cretaceous. GSA Bulletin 135, 712–724. https://doi.org/10.1130/B36340.1.

Wu, H., Zhang, S., Hinnov, L.A., Jiang, G., Yang, T., Li, H., Wan, X., Wang, C., 2014. Cyclostratigraphy and orbital tuning of the terrestrial upper Santonian–Lower Danian in Songliao Basin, northeastern China. Earth Planet Sci. Lett. 407, 82–95. https://doi.org/10.1016/j.epsl.2014.09.038.

Wu, H., Zhang, S., Jiang, G., Huang, Q., 2009. The floating astronomical time scale for the terrestrial Late Cretaceous Qingshankou Formation from the Songliao Basin of Northeast China and its stratigraphic and paleoclimate implications. Earth Planet Sci. Lett. 278, 308–323. https://10.1016/j.epsl.2008.12.016.

Xi, D., Cao, W., Huang, Q., Do Carmo, D.A., Li, S., Jing, X., Tu, Y., Jia, J., Qu, H., Zhao, J., Wan, X., 2016. Late Cretaceous marine fossils and seawater incursion events in the Songliao Basin, NE China. Cretac. Res. 62, 172–182. https://doi.org/10.1016/j.cretres.2015.10.025.

Xiao, H., Li, M.J., Nettersheim, B.J., You, B., Lu, M., Cheng, D.S., 2025. Late Cretaceous marine incursion into central Africa. Pet. Sci. 22, 1811–1822. https://10.1016/j.petsci.2025.02.022.

Xu, J., Liu, Z., Bechtel, A., Meng, Q., Sun, P., Jia, J., Cheng, L., Song, Y., 2015. Basin evolution and oil shale deposition during Upper Cretaceous in the Songliao Basin (NE China): Implications from sequence stratigraphy and geochemistry. Int. J. Coal Geol. 149, 9–23. https://doi.org/10.1016/j.coal.2015.07.005.

Xu, J., Liu, Z., Bechtel, A., Sachsenhofer, R.F., Jia, J., Meng, Q., Sun, P., 2019. Organic matter accumulation in the Upper Cretaceous Qingshankou and Nenjiang formations, Songliao Basin (NE China): Implications from high-resolution geochemical analysis. Mar. Petrol. Geol. 102, 187–201. https://doi.org/10.1016/j.marpetgeo.2018.12.037.

Zhang, P., Misch, D., Meng, Q., Sachsenhofer, R.F., Liu, Z., Jia, J., Gao, F., Bechtel, A., Hu, F., 2022. Lateral changes of organic matter preservation in the lacustrine Qingshankou Formation (Cretaceous Songliao Basin, NE China): Evidence for basin segmentation. Int. J. Coal Geol. 254, 103984. https://10.1016/j.coal.2022.103984.

Zhang, S.C., Wang, H.J., Liu, Y.K., Wang, X.M., Liu, H., Sun, L.D., 2024. Lacustrine carbon sink: A hidden driver of the Late Cretaceous Cooling Event. Sci. Bull. 69, 3949–3958. https://10.1016/j.scib.2024.06.024.

Zhu, X.M., Cao, J., Xia, L.W., Bian, L.Z., Liu, J.C., Zhang, R.J., 2023. Links between marine incursions, lacustrine anoxic and organic matter enrichment in the Upper Cretaceous Qingshankou Formation, Songliao Basin, China. Mar. Petrol. Geol. 158, 106536. https://10.1016/j.marpetgeo.2023.106536.

Zou, C., Qiu, Z., Zhang, J., Li, Z., Wei, H., Liu, B., Zhao, J., Yang, T., Zhu, S., Tao, H., Zhang, F., Wang, Y., Zhang, Q., Liu, W., Liu, H., Feng, Z., Liu, D., Gao, J., Liu, R., Li, Y., 2022. Unconventional petroleum sedimentology: A key to understanding unconventional hydrocarbon accumulation. Engineer 18, 62–78. https://doi.org/10.1016/j.eng.2022.06.016.

Zou, C.N., Yang, Z., Cui, J.W., Zhu, R.K., Hou, L.H., Tao, S.Z., Yuan, X.J., Wu, S.T., Lin, S.H., Wang, L., Bai, B., Yao, J.L., 2013. Formation mechanism, geological characteristics and development strategy of nonmarine shale oil in China. Petrol. Explor. Dev. 40, 15–27. https://10.1016/s1876-3804(13)60002-6.